Full-field Calculation of Hole Drilling Residual Stresses from Electronic Speckle Pattern Interferometry Data

by G.S. Schajer and M. Steinzig

ABSTRACT—A mathematical method is proposed for calculating residual stresses from hole drilling electronic speckle pattern interferometry (ESPI) data, independent of rigid-body motions. Even though the signal-to-noise ratio of typical ESPI data is modest, the method achieves good computational stability by averaging a large amount of data. It does this without excessive numerical effort by exploiting known trigonometric relationships among the data. The resulting stress calculations are very rapid, and are well suited for future application to non-uniform stress measurements.

KEY WORDS—Residual stress, hole drilling, ESPI, laser holography, inverse solution

Introduction

Practical convenience, reliability, and modest damage to the test specimen makes the hole drilling method an attractive choice for measuring residual stresses in materials. The measurement principle was introduced in 1934 by Mathar.[1] However, the mechanical extensometer that was originally used did not provide a very stable measure of surface deformations. The subsequent application of strain gages[2,3] greatly improved the accuracy and reliability of the measurements. Now, the strain gage procedure is formalized as an American Society for Testing and Materials (ASTM) Standard Test Method.[4]

Electronic speckle pattern interferometry (ESPI)[5,6] provides additional opportunities for measuring surface displacements for the hole drilling method.[7] The non-contact nature of the technique avoids the significant time taken to install strain gages, associated wiring and surface coatings. In addition, ESPI provides a much richer, full-field data set than is available from strain gages. However, the benefits of this "richness" are only realized if an effective mathematical method can be used to extract a small number of results, typically the three in-plane stress components, from among the many thousands of available ESPI data. This challenge is compounded by the presence of significant noise among the measurements.

Nelson and co-workers[7,8] introduced the use of three pairs of diametrally opposite points for evaluating residual stresses. This method was subsequently generalized to the use of many manually selected points by Schmitt and Hunt.[9] The increased number of data used improves averaging, reduces noise, and enhances calculation accuracy. In another approach, Focht and Schiffner[10] used all the data along a concentric circular line surrounding the hole, thus avoiding the manual data selection. Most recently, Steinzig and Ponslet[11] presented a least-squares procedure that uses the entire set of available surface displacements, thereby greatly increasing data averaging and significantly enhancing calculation accuracy. However, the associated calculations are numerically intensive, and become substantially more so when extended to non-uniform residual stress evaluation.

In this paper we present an alternative numerical technique for calculating residual stresses from ESPI data. The proposed method uses most of the available data and therefore retains the averaging advantage. It achieves substantial computational economy by exploiting known mathematical relationships within the measured data. This approach enables the many thousands of displacement data to be reduced to a small number (typically 3–10) of representative values, from which the associated residual stresses can be calculated. The small number of these quantities greatly reduces the numerical effort required and makes the method practicable for non-uniform residual stress calculations.

ESPI Measurements

The ESPI technique is well documented elsewhere[5,6,12,13] and will be only briefly summarized here. Figure 1 schematically shows a typical ESPI setup. The light from a laser source is split using a half-silvered mirror. One part passes through a piezoelectric actuator to provide a phase-stepped reference light to a CCD camera. The other part of the laser light (the "illumination beam") is used to illuminate the specimen, which is imaged (the "object beam") through a zoom lens onto the CCD. The object beam interferes with the reference light to produce a speckle pattern on the CCD, the local phase of which varies with displacement of the specimen surface. By taking a series of phase-stepped images before and after surface deformation, it is possible to evaluate both the size and sign of the deformation at every pixel in the CCD image. The data at each pixel correspond to the component of the three-dimensional surface deformation in the direction of the "sensitivity vector". This vector bisects the directions of the illumination and object beams. In the present

---

G.S. Schajer (SEM member; schajer@mech.ubc.ca) is a Professor, Department of Mechanical Engineering, University of British Columbia, Vancouver, Canada. M. Steinzig (SEM member) was a Vice-President, Hytec Inc., 110 Eastgate Drive, Los Alamos, New Mexico, USA. M. Steinzig is now at Los Alamos National Laboratory, Los Alamos, New Mexico, USA.

Original manuscript submitted: January 21, 2005.
Final manuscript received: June 4, 2005.
DOI: 10.1177/0014485105059553

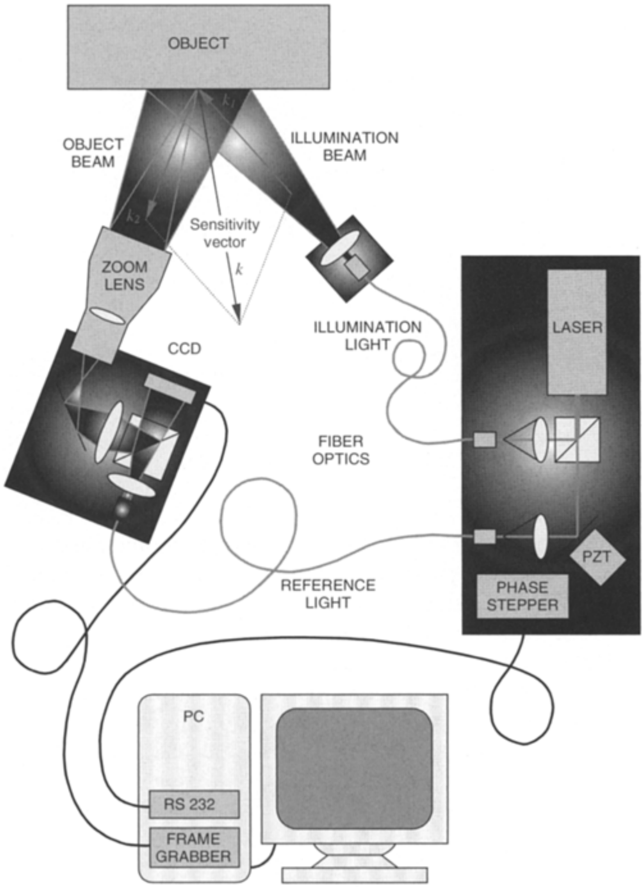

Fig. 1—Schematic diagram of the ESPI setup (reproduced from Steinzig and Ponslet[11])

application, the image contains the area around the drilled hole, and the measured deformations are those caused by hole drilling.

Hole Drilling Deformations

Figure 2 schematically shows a circular hole of radius a drilled into a specimen subject to in-plane residual stress components σ_x, σ_y, and τ_{xy}. As a result of hole drilling, the specimen surface around the hole deforms in three dimensions. For each surface point, there are axial, radial, and circumferential displacement components.

For in-plane loadings around an axisymmetric feature such as a circular hole, it is convenient to transform the axial residual stresses into equivalent isotropic and shear stresses:[14]

$$P = (\sigma_x + \sigma_y)/2, \quad Q = (\sigma_x - \sigma_y)/2, \quad T = \tau_{xy}. \quad (1)$$

This transformation is useful because, for linear elastic material properties, the associated deformations have simple trigonometric forms. The trigonometric relationships in the following equations are "exact",[15] and not approximate as sometimes reported.

For isotropic loading, P acting alone, the deformations are

$$U_z(r,\theta) = u_z(r), \quad U_r(r,\theta) = u_r(r), \quad U_\theta(r,\theta) = 0, \quad (2)$$

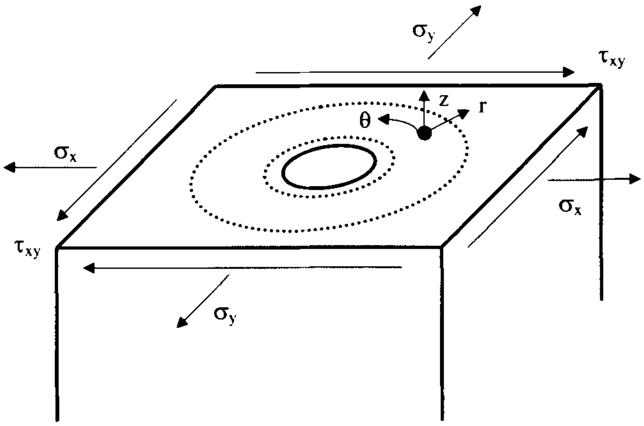

Fig. 2—Hole drilling residual stress geometry

where $U_z(r,\theta)$ is the axial (out-of-plane) displacement at a surface point with cylindrical coordinates (r,θ). $u_z(r)$ is the radial profile of the axial displacement. This profile can be evaluated by finite element analysis.[14,15] The first two equations of eq (2) indicate that the axial and radial displacements $U_z(r,\theta)$ and $U_r(r,\theta)$ are independent of angle θ, i.e., it is axisymmetric. This is as expected because the isotropic loading associated with P is non-directional. For this axisymmetric case, all circumferential displacements $U_\theta(r,\theta)$ are zero.

For shear loading at 45° to the x–y axes, Q acting alone, the deformations are

$$V_z(r,\theta) = v_z(r)\cos 2\theta, \quad V_r(r,\theta) = v_r(r)\cos 2\theta,$$
$$V_\theta(r,\theta) = -v_\theta(r)\sin 2\theta, \quad (3)$$

where $V_z(r,\theta)$ is the axial displacement corresponding to Q, and $v_z(r)$ is the profile of axial displacements along the radius at $\theta = 0$. Analogous trigonometric relationships apply to the radial and circumferential displacements.

Similar equations apply for shear loading in the axial directions, T acting alone,

$$V_z^*(r,\theta) = v_z(r)\sin 2\theta, \quad V_r^*(r,\theta) = v_r(r)\sin 2\theta,$$
$$V_\theta^*(r,\theta) = v_\theta(r)\cos 2\theta, \quad (4)$$

where the superscript * is added instead of using a separate symbol to indicate that the deformations for T loading are essentially the same as for Q, but with a rotation of 45°.

In addition to the above elastic deformations, ESPI measurements may also include arbitrary rigid-body motions caused by small relative movements of the components in Fig. 1. Local temperature change and bulk movement of the part caused by drilling are common causes of these movements. These rigid-body motions include translation and rotation about the x and y axes. The corresponding axial displacements are

$$W(r,\theta) = w_0 + w_1 r/a\cos\theta + w_2 r/a\sin\theta, \quad (5)$$

where w_0, w_1, and w_2, respectively, are the normalized amplitudes of the rigid-body translation and rotations around the x and y axes at $r = a$.

The Cartesian components of the surface displacements for the combination of cases described by eqs (2)–(5) are

$$
\begin{aligned}
d(r,\theta) &= \frac{P}{E}\begin{pmatrix} U_r(r,\theta)\cos\theta i + U_r(r,\theta)\sin\theta j \\ +U_z(r,\theta)\,k \end{pmatrix} \\
&+\frac{Q}{E}\begin{pmatrix} V_r(r,\theta)\cos\theta i - V_\theta(r,\theta)\sin\theta i \\ +V_r(r,\theta)\sin\theta j + V_\theta(r,\theta)\cos\theta j \\ +V_z(r,\theta)\,k \end{pmatrix} \\
&+\frac{T}{E}\begin{pmatrix} V_r^*(r,\theta)\cos\theta\, i - V_\theta^*(r,\theta)\sin\theta i \\ +V_r^*(r,\theta)\sin\theta\, j + V_\theta^*(r,\theta)\cos\theta j \\ +V_z^*(r,\theta)\,k \end{pmatrix} \\
&+\left(w_0 + w_1\,\tfrac{r}{a}\cos\theta + w_2\,\tfrac{r}{a}\sin\theta\right)k
\end{aligned} \tag{6}
$$

where $\boldsymbol{i}, \boldsymbol{j}$, and $\boldsymbol{k}$ are unit vectors in the x–y–z directions. The normalization with respect to Young's modulus in eq (6) allows the displacements $U_r(r,\theta)$, etc., to be expressed in dimensionless form. However, these quantities are not completely material-independent because there remain complex dependences on Poisson's ratio. Although some approximation of this dependence is possible,[16] to be more conservative, a numerical scheme was adopted here to interpolate between displacements calculated at discrete values of Poisson's ratio.

Residual Stress Calculation Method

The ESPI observed surface displacement $D(r,\theta)$ is the component of the surface displacement vector $\boldsymbol{d}(r,\theta)$ in the direction of the sensitivity vector $\boldsymbol{c} = c_x\,\boldsymbol{i} + c_y\,\boldsymbol{j} + c_z\,\boldsymbol{k}$. The direction of this vector bisects the directions of the illumination and object beams in Fig. 1. Combining eqs (2)–(6), and using trigonometric identities gives the ESPI observed surface displacement:

$$
\begin{aligned}
D(r,\theta) &= d(r,\theta)\bullet c \\
&= \frac{P}{2E}\left\{\begin{array}{l} 2\left(c_x\cos\theta + c_y\sin\theta\right)u_r(r) \\ +2c_z u_z(r) \end{array}\right\} \\
&+\frac{Q}{2E}\left\{\begin{array}{l} \left[\left(c_x\cos\theta - c_y\sin\theta\right)\right. \\ \left.+\left(c_x\cos 3\theta + c_y\sin 3\theta\right)\right] v_r(r) \\ +\left[\left(c_x\cos\theta - c_y\sin\theta\right)\right. \\ \left.-\left(c_x\cos 3\theta + c_y\sin 3\theta\right)\right] v_\theta(r) \\ +2c_z\cos 2\theta v_a(r) \end{array}\right\} \\
&+\frac{T}{2E}\left\{\begin{array}{l} \left[\left(c_x\sin\theta + c_y\cos\theta\right)\right. \\ \left.+\left(c_x\sin 3\theta - c_y\cos 3\theta\right)\right] v_r(r) \\ +\left[\left(c_x\sin\theta + c_y\cos\theta\right)\right. \\ \left.-\left(c_x\sin 3\theta - c_y\cos 3\theta\right)\right] v_\theta(r) \\ +2c_z\sin 2\theta v_z(r) \end{array}\right\} \\
&+\left(w_0 + w_1\,\tfrac{r}{a}\cos\theta + w_2\,\tfrac{r}{a}\sin\theta\right)c_z.
\end{aligned} \tag{7}
$$

In eq (7), the displacement field $D(r,\theta)$ is experimentally determined, and the quantities $u_r(r)$, etc., are known through finite element calculations. The objective is to calculate the residual stresses P, Q, and T (and possibly rigid-body motions w_0, w_1, and w_2). The mathematical challenge (and opportunity) is to evaluate these few quantities from the many thousands of measured data $D(r,\theta)$.

Despite its substantial length, eq (7) is algebraically simple. It retains in linear form the trigonometric characteristics of its origin in eq (6). This feature makes eq (7) amenable to Fourier analysis, by which means it can be divided into manageable parts. In addition, and very importantly, the Fourier method reduces the thousands of measured $D(r,\theta)$ data to a much smaller number of representative quantities.

The analysis proceeds from the orthogonality properties of the trigonometric functions:

$$
\begin{aligned}
\int_0^{2\pi}\cos n\theta\cos m\theta\,\mathrm{d}\theta &= \begin{array}{c} 2\pi \text{ for } m = n = 0 \\ \pi \text{ for } m = n \neq 0 \\ 0 \text{ otherwise} \end{array} \\
\int_0^{2\pi}\sin n\theta\sin m\theta\,\mathrm{d}\theta &= \begin{array}{c} \pi \text{ for } m = n \neq 0 \\ 0 \text{ otherwise} \end{array} \\
\int_0^{2\pi}\cos n\theta\sin m\theta\,\mathrm{d}\theta &= \quad 0 \text{ always.}
\end{aligned} \tag{8}
$$

The solution procedure involves weighting the measured $D(r,\theta)$ data using a trigonometric function, say $\cos 2\theta$, and integrating over an annular region around the hole bounded by inner and outer radii r_1 and r_2. These radii are chosen so that they enclose the region of significant surface displacement. All the integrals corresponding to the individual terms in eq (7), except the one containing $\cos 2\theta$, equal zero because of the orthogonality properties in eq (8). Equation (7) reduces to

$$
\int_{r_1}^{r_2}\int_0^{2\pi} D(r,\theta)\,r\,\mathrm{d}r\,\mathrm{d}\theta = \frac{\pi Q}{E}\int_{r_1}^{r_2} v_z(r)\,r\,\mathrm{d}r \tag{9}
$$

from which Q can be evaluated explicitly. A similar calculation using $\sin 2\theta$ as a weighting function yields T. However, there is no similar direct way of evaluating P because all associated trigonometric terms also appear elsewhere in eq (7). Even without this limitation, it turns out that eq (9) is not an ideal way of proceeding because the calculation uses only the axial displacements $v_z(r)$. These displacements are much smaller than the in-plane displacements $v_r(r)$ and $v_\theta(r)$, and so are more sensitive to measurement noise. A different approach is therefore required.

The idea of using orthogonality to divide the terms in eq (7) can be generalized beyond the direct application in eq (9). When carrying out practical calculations, it is useful to define the following dimensionless "calibration constants":

$$
\begin{aligned}
A_z &= \frac{1}{a\left(r_2^2 - r_1^2\right)}\int_{r_1}^{r_2} f(r)\,u_z(r)\,r\,\mathrm{d}r \\
A_r &= \frac{1}{a\left(r_2^2 - r_1^2\right)}\int_{r_1}^{r_2} f(r)\,u_r(r)\,r\,\mathrm{d}r \\
B_z &= \frac{1}{a\left(r_2^2 - r_1^2\right)}\int_{r_1}^{r_2} f(r)\,v_z(r)\,r\,\mathrm{d}r \\
B_r &= \frac{1}{a\left(r_2^2 - r_1^2\right)}\int_{r_1}^{r_2} f(r)\,v_r(r)\,r\,\mathrm{d}r \\
B_\theta &= \frac{1}{a\left(r_2^2 - r_1^2\right)}\int_{r_1}^{r_2} f(r)\,v_\theta(r)\,r\mathrm{d}r.
\end{aligned} \tag{10}
$$

A radial weighting function $f(r)$ is included in eq (10) to provide for future mathematical needs. The displacement profiles $u_z(r)$, etc., can be determined from finite element calculations, and $f(r)$ and other quantities are explicitly known. Thus, A_z, A_r, etc., reduce to dimensionless numbers. These "calibration constants" are functions of hole depth and Poisson's ratio, and appropriate values of these latter two quantities must be used for the associated finite element calculations. However, these calculations need only be done once. The results can be organized in tabular form, from which future needed values can be extracted by interpolation.

The following weighted integrals of the measured data are useful

$$
\begin{aligned}
C0 &= \frac{1}{2\pi a(r_2^2-r_1^2)} \int_{r_1}^{r_2} \int_{0}^{2\pi} f(r)\, D(r,\theta)\, r \,\mathrm{d}r\, \mathrm{d}\theta \\
C1 &= \frac{1}{\pi a(r_2^2-r_1^2)} \int_{r_1}^{r_2} \int_{0}^{2\pi} f(r)\, D(r,\theta) \cos\theta\, r \,\mathrm{d}r\, \mathrm{d}\theta \qquad (11) \\
S1 &= \frac{1}{\pi a(r_2^2-r_1^2)} \int_{r_1}^{r_2} \int_{0}^{2\pi} f(r)\, D(r,\theta) \sin\theta\, r \,\mathrm{d}r\, \mathrm{d}\theta
\end{aligned}
$$

and similarly for analogous integrals using cos 2θ, sin 2θ, cos 3θ, and sin 3θ as circumferential weighting functions. In eq (11), the radial weighting functions $f(r)$ are the same as chosen for use in eq (10). The additional factor 2 in the definition of $C0$ corresponds to the same factor appearing in the first of the orthogonality conditions (8).

In practice, eqs (11) are evaluated from CCD data, which are in discrete pixel format. In terms of pixels, the second equation of eqs (11) becomes

$$C1 = \frac{1}{N} \sum_{i=1}^{N} f(r_i)\, D_i \cos\theta_i \qquad (12)$$

where i is a pixel index and N is the number of pixels within the integration area. The other integrals can be evaluated in the same way. Equations (10) and (11) were defined including a division by the integration area to normalize eq (12) and to make it independent of pixel density.

The main obstacle to the direct extraction of P, Q, and T from eq (7) is the sharing of trigonometric terms with the rigid-body motions w_0, w_1, and w_2. This obstacle can be removed by generalizing the orthogonality idea contained in eq (8) to the radial direction, by requiring

$$\int_{r_1}^{r_2} f(r)\, r\, \mathrm{d}r = 0. \qquad (13)$$

Use of an appropriate weighting function eliminates the integral associated with the w_0 term. Any function $f(r)$ obeying eq (13) is acceptable. Here, a simple polynomial is chosen

$$
\begin{aligned}
& f(r) = \tfrac{a}{r} - \beta \\
& \text{where for } C0,\ C2 \text{ and } S2\ \beta = \tfrac{2a}{r_1+r_2} \qquad (14) \\
& \text{and for } C1,\ S1,\ C3 \text{ and } S3\ \beta = \tfrac{3a(r_1+r_2)}{2(r_1^2+r_1r_2+r_2^2)}\ .
\end{aligned}
$$

The two different values for β shown in eq (14) are chosen to accommodate the additional factor r in the w_1 and w_2 terms of eq (7). The first value of β in eq (14) is used for the out-of-plane constants in eq (10), and for the even numbered integrals in eqs (11) and (12). The second value of β is used for the in-plane constants in eq (10), and for the odd numbered integrals in eqs (11) and (12).

There are seven different trigonometric terms in eq (7), and so seven weighted integrals can be evaluated. Using the quantities defined in eqs (10) and (12), the results of the seven integrations can be expressed compactly in matrix form:

$$
\left[\begin{array}{ccc}
c_z A_z & 0 & 0 \\
0 & c_z B_z & 0 \\
0 & 0 & c_z B_z \\
\hline
c_x A_r & c_x B_r & c_x B_\theta \\
c_x A_r & c_x B_\theta & c_y B_r \\
c_y A_r & -c_y B_\theta & c_x B_r \\
c_y A_r & -c_y B_r & c_x B_\theta
\end{array}\right]
\left[\begin{array}{c} P/E \\ Q/E \\ T/E \end{array}\right]
=
\left[\begin{array}{c}
C0 \\ C2 \\ S2 \\
\hline
C1 + C3 \\ C1 - C3 \\ S1 + S3 \\ S1 - S3
\end{array}\right] . \qquad (15)
$$

The three rows above the dashed dividing line refer to out-of-plane displacements, and the four rows below refer to in-plane displacements. Three unknowns, P, Q, and T are required, and a total of seven equations are available. A solution can be found using any three rows. The upper three rows form a diagonal matrix, and therefore provide a particularly simple solution. However, as already observed, the associated out-of-plane displacements are relatively small and consequently are more sensitive to measurement noise. Choosing from among the lower (in-plane) rows gives a better solution. Even better is to choose all the rows because this more fully uses the available data. The least-squares method[17] provides a convenient way of achieving that objective. The procedure involves pre-multiplying both sides of eq (15) by the transpose of the left-side matrix to form the "normal equations". These comprise a 3 × 3 matrix equation whose solutions are P, Q, and T. The Cartesian stresses can then be determined using

$$\sigma_x = P + Q, \quad \sigma_y = P - Q, \quad \tau_{xy} = T. \qquad (16)$$

Rigid-body Motion Calculation

The principal objective of hole drilling is to determine the residual stresses in the specimen. The presence of rigid-body motions is an unwanted artifact whose effects need to be excluded from the evaluation. The radial orthogonality in eq (13) excludes rigid-body motion effects at source, causing the associated variables to be entirely absent from eq (15). However, for some applications, it is useful to know the rigid-body motions explicitly, and for this case, eq (15) is not suitable.

Rigid-body motion is retained simply by not enforcing radial orthogonality, for example by using a weighing function that does not obey eq (13). The resulting formulation gives a set of seven equations similar to eq (15), but with the unknowns increased to six with the inclusion of w_0, w_1, and w_2. However, even though there are more equations than unknowns, this procedure does not provide a solution because the resulting normal equations are singular. A similar singularity was observed by Focht and Schiffner[10] when performing calculations using data along a circular line.

The singularity suggests that the information content of the data is not being fully used. One way of extracting further information is to use several different weighting functions. These can be chosen to be similar in shape to the physical cases to which they correspond. For example, all the displacement profiles $u_z(r)$, $u_r(r)$, etc., have shapes that are approximately inversely proportional to radius. Thus, $f(r) = a/r$ is an appropriate choice for associated calculations. Similarly, the rigid-body rotations w_1 and w_2 are proportional to radius, so $f(r) = r/a$ is an appropriate choice for these terms. Likewise, $f(r) = 1$ is appropriate for rigid-body displacements associated with w_0. To accommodate these extensions, the notations in eqs (10) and (12) need to be expanded. Superscript numbers in brackets following the symbols A_z, $C0$, etc., indicate the power of normalized radius used for the weighting function. For example, A_z evaluated with $f(r) = a/r$ is written $A_z[-1]$. Using this notation, eq (15) can be expanded to

$$\begin{bmatrix} c_zA_z^{[-1]} & 0 & 0 & K_1 & 0 & 0 \\ 0 & c_zB_z^{[-1]} & 0 & 0 & 0 & 0 \\ 0 & 0 & c_zB_z^{[-1]} & 0 & 0 & 0 \\ c_xA_r^{[-1]} & c_xB_r^{[-1]} & c_yB_\theta^{[-1]} & 0 & K_2 & 0 \\ c_xA_r^{[-1]} & c_xB_\theta^{[-1]} & c_yB_r^{[-1]} & 0 & K_2 & 0 \\ c_yA_r^{[-1]} & -c_yB_\theta^{[-1]} & c_xB_r^{[-1]} & 0 & 0 & K_2 \\ c_yA_r^{[-1]} & -c_yB_r^{[-1]} & c_xB_\theta^{[-1]} & 0 & 0 & K_2 \\ c_zA_z^{[0]} & 0 & 0 & K_2 & 0 & 0 \\ c_xA_r^{[1]} & c_xB_r^{[1]} & c_yB_\theta^{[1]} & 0 & K_4 & 0 \\ c_xA_r^{[1]} & c_xB_\theta^{[1]} & c_yB_r^{[1]} & 0 & K_4 & 0 \end{bmatrix} \begin{bmatrix} P/E \\ Q/E \\ T/E \\ w_0/a \\ w_1/a \\ w_2/a \end{bmatrix} = \begin{bmatrix} C0^{[-1]} \\ C2^{[-1]} \\ S2^{[-1]} \\ C1^{[-1]} + C3^{[-1]} \\ C1^{[-1]} - C3^{[-1]} \\ S1^{[-1]} + S3^{[-1]} \\ S1^{[-1]} - S3^{[-1]} \\ C0^{[0]} \\ C1^{[1]} + C3^{[1]} \\ C1^{[1]} - C3^{[1]} \end{bmatrix}, \qquad (17)$$

where $K_1 = c_z/(r_2 + r_1)$, $K_2 = c_z/2$ and $K_4 = c_z(r_2^4 - r_1^4)/4a^2(r_2^2 - r_1^2)$. Equation (17) gives full-rank normal equations, from which all of P, Q, T, w_0, w_1, and w_2 can be determined. Although the values of P, Q, and T evaluated from eq (15) are not numerically identical to those from eq (17), they are almost so.

Test Calculations

The above described calculations were tested on some experimental hole drilling measurements made using a PRISM-RS laser interferometry system (Hytec, Inc., NM). The arrangement of this equipment follows the schematic plan shown in Fig. 1. Steinzig and Ponslet[11] and Steinzig et al.[18] give details of the measurement procedure. A bent beam assembly of the type described in Steinzig et al.[18] was used to create a specimen with known residual stresses. A 1.59 mm diameter hole, 0.5 mm deep, was drilled in the specimen surface. ESPI measurements as described in Steinzig and Ponslet[11] were made both before and after drilling the hole. For these measurements, the illumination beam was aligned at 66° from the specimen normal, and the object beam was on the same side at 49°. This arrangement was chosen to provide optical clearance for the drill used to cut the hole.

Figure 3(a) shows the measured phase map around the drilled hole. The light and dark fringes correspond to sequential half-wavelength displacements along the sensitivity direction. Noise in the measured data causes the grainy texture of the fringes. The central curve in Fig. 3(a) indicates the hole of radius a. The two dashed curves indicate the annular integration boundaries at radii $r_1/a = 2.0$ and $r_2/a = 4.0$. Although all these curves are concentric circles on the specimen surface, they appear as ellipses in Fig. 3(a) because the object beam was not normal to the specimen surface. However, the resulting coordinate transformation in the phase map does not create any difficulties. After identifying the specimen-based coordinate (r, θ) for each pixel, eq (12) can be used directly. The normalization by the total number of pixels, N, removes the need for any further scaling of dimensions.

Table 1 summarizes the stresses calculated from the phase map in Fig. 3(a). The results show that the proposed calculation method gives residual stress values in good agreement with the experimental expectations. Equations (17) and (15) give very similar but not identical results. The subsequent "in-plane" calculations use only the lower four rows of eq (15), while the "out-plane" results use only the upper four rows. In general, the "out-plane" results are less reliable than the others because of the modest size of the out-of-plane displacements. They are particularly unreliable here because, in addition, the displacement sensitivity vector has only a small out-of-plane component. Stress evaluations performed using eqs (15) and (17) likely have similar accuracies, and are preferred over "in-plane" and "out-plane" calculations because of their greater data content. Equation (15) has the advantage of being more numerically efficient, while eq (17) is able to determine the rigid-body motions.

The results from eq (17) indicate that the some rigid-body motions have occurred. Zero displacement shows as a white area in Fig. 3(a). The dark areas in the far-field away from the hole, where zero displacements are expected, indicate the presence of significant rigid-body motions. As a test of the rigid-body motion calculation provided by eq (17), the calculated rigid-body motions were subtracted from the data in Fig. 3(a). The result in Fig. 3(b) shows the expected brighter areas in the far-field.

As a further test of eq (17), the calculated stress-induced displacements were also subtracted. The "residual" plot in Fig. 3(c) shows a uniform bright area, indicating that the stress solution was successful at modeling the ESPI data. The area immediately adjacent to the hole appears darker, suggesting that some displacements were not determined by the calculation. However, further investigation revealed these pixels are mostly decorrelated, and do not contain useful information. This decorrelation can be seen in Figs. 3(a) and (b) because

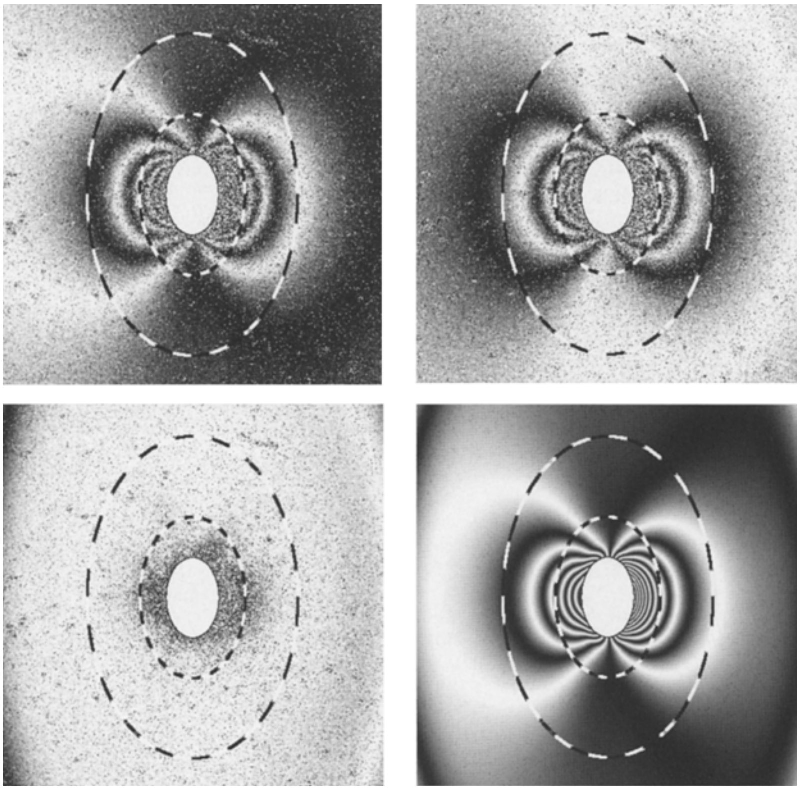

Fig. 3—Phase maps around the drilled hole, with integration radii $r_1/a = 1.33$ and $r_2/a = 4.0$: (a) measured data; (b) measured data minus rigid-body motions; (c) residuals after subtracting theoretical model; (d) theoretical model

TABLE 1—CALCULATED RESIDUAL STRESSES FOR THE PHASE MAP IN FIG. 3

Method	x-stress (MPa)	y-stress (MPa)	xy-stress (MPa)	Displacement (μm)	x-rotation (μm)	y-rotation (μm)
Expected	207	0	0	–	–	–
eq (17)	193	–4	–2	0.174	–0.002	0.008
eq (15)	193	–2	–4	–	–	–
eq (15) (in-plane)	193	–2	–4	–	–	–
eq (15) (out-plane)	332	–70	–56	–	–	–
Least-squares	194	–2	–3	0.174	–0.001	0.008

the fringe pattern does not extend right up to the hole boundary. Instead, it fades out close to the inner integration radius. This radius was chosen here at $r_1/a = 2.0$ as a compromise between excluding the decorrelated pixels near the hole, and including the immediately adjacent information-rich, high-displacement pixels. The reason for the decorrelation is not clear. It may perhaps be due to abrasion of the surface by the passage of chips cut from the hole.

The choice of outer integration radius in Fig. 3 also involves a compromise. This radius should be large enough to enhance data averaging by including many pixels within the annular integration area. However, it should not be excessive because the surface displacements far from the hole are relatively small, and the information content of the far-field pixels rapidly diminishes with radial position. A suitable range for the outer integration radius is $r_2/a = 3.5 - 5.0$.

Figure 3(d) shows the theoretical fringe pattern corresponding to the stresses and rigid-body motions calculated by eq (17). The result successfully reproduces the experimentally measured fringe pattern in Fig. 3(a), and provides a further confirmation of the proposed calculation method. (Note that Fig. 3a equals Fig. 3d plus Fig. 3c.) The theoretical data are smooth and do not have the grainy texture of the experimental data. The experimental graininess is caused by optical noise, an artifact that the proposed calculation method counteracts by averaging many pixels. Using data from within the integration area of the residual plot in Fig. 5, the root-mean-square (rms) of the noise is 0.030 μm. This compares with the rms of the "signal" (the theoretical data corresponding to Fig. 3b) of 0.209 μm, giving a signal-to-noise ratio of 7.0. This modest ratio confirms the need for the substantial data averaging that is a major feature of the calculation method presented here.

Conclusions

The mathematical method proposed here is an effective and practical procedure for calculating residual stresses from hole drilling ESPI data, independent of rigid-body motions associated with hole drilling or temperature changes. Even though the signal-to-noise ratio of typical ESPI data is modest, the method achieves good computational stability by averaging a large amount of data. It does this without excessive numerical effort by exploiting the known trigonometric relationships among the data. The resulting stress calculations are very rapid, taking less than 1 s using an ordinary desktop computer. This feature makes it practicable to extend the calculation method to non-uniform stress measurements. This extension will be reported in a future publication.

Acknowledgments

This work was supported by the Natural Sciences and Engineering Research Council of Canada (NSERC). Hytec, Inc., Los Alamos, NM, kindly provided the experimental equipment and use of facilities.

References

1. *Mathar, J., "Determination of Initial Stresses by Measuring the Deformations Around Drilled Holes," Transactions of the ASME, Iron Steel,* **56** *(2), 249–254 (1934).*

2. *Soete, W. and Vancrombrugge, R., "An Industrial Method for the Determination of Residual Stresses, Proceedings of SESA,* **8** *(1), 17–28 (1950).*

3. *Rendler, N.J. and Vigness, I., "Hole Drilling Strain-gage Method of Measuring Residual Stresses," EXPERIMENTAL MECHANICS,* **6** *(12), 577–586 (1966).*

4. *American Society for Testing and Materials, "Standard Test Method for Determining Residual Stresses by the Hole Drilling Strain-Gage Method," ASTM E837-01, American Society for Testing and Materials, West Conshohocken, PA (2001).*

5. *Butters, J.N. and Leendertz, J.A., "Holographic and Video Techniques Applied to Engineering Measurements," Journal of Measurement and Control,* **4** *(12), 349–354 (1971).*

6. *Macovski, A., Ramsey, S.D., and Schaefer, L.F., "Time-lapse Interferometry and Contouring Using Television Systems," Applied Optics,* **10**, *2722–2727 (1971).*

7. *Nelson, D.V. and McCrickerd, J.T., "Residual-stress Determination Through Combined Use of Holographic Interferometry and Blind-Hole Drilling," EXPERIMENTAL MECHANICS,* **26** *(4), 371–378 (1986).*

8. *Makino, A. and Nelson, D., "Residual-stress Determination by Single-axis Holographic Interferometry and Hole Drilling – Part I: Theory," EXPERIMENTAL MECHANICS,* **34** *(1), 66–78 (1994).*

9. *Schmitt, D.R. and Hunt, R.W., "Inversion of Speckle Interferometer Fringes for Hole Drilling Residual Stress Determinations," EXPERIMENTAL MECHANICS,* **40** *(2), 129–137 (2000).*

10. *Focht, G. and Schiffner, K., "Determination of Residual Stresses by an Optical Correlative Hole Drilling Method," EXPERIMENTAL MECHANICS,* **43** *(1), 97–104 (2003).*

11. *Steinzig, M. and Ponslet, E., "Residual Stress Measurement using the Hole Drilling Method and Laser Speckle Interferometry: Part I," Experimental Techniques,* **27** *(3), 43–46 (2003).*

12. *Jones, R. and Wykes, C., Holographic and Speckle Interferometry, 2nd edition, Cambridge University Press, Cambridge (1989).*

13. *Cloud, G.L., Optical Methods of Engineering Analysis, Cambridge University Press, Cambridge (1995).*

14. *Schajer, G.S., "Measurement of Non-uniform Residual Stresses Using the Hole Drilling Method. Part I – Stress Calculation Procedures," Journal of Engineering Materials and Technology,* **110** *(4), 338–343 (1988).*

15. *Zienkiewicz, O.C., The Finite Element Method, 3rd edition, Chapter 15, McGraw-Hill, New York (1977).*

16. *Rumzan, I. and Schmitt, D.R., "Three-dimensional Stress-relief Displacements from Blind-hole Drilling: A Parametric Description," EXPERIMENTAL MECHANICS,* **43** *(1), 52–60 (2003).*

17. *Dahlquist, G., Björk, Å., and Anderson, N., Numerical Methods, Chapter 4, Prentice-Hall, Englewood Cliffs, NJ (1974).*

18. *Steinzig, M., Hayman, G.J., and Prime, M.B., "Verification of a Technique for Holographic Residual Stress Measurement," Residual Stress Measurement and General Non-destructive Evaluation, PVP Vol. 429, D.E. Bray, editor, ASME Pressure Vessels and Piping Conference, Atlanta, GA, July 23–26 (2001).*